PNAS RESEARCH ARTICLE | APPLIED PHYSICAL SCIENCES

Calibration-free, high-precision, and robust terahertz ultrafast metasurfaces for monitoring gastric cancers

Jing Lou[a,b,c,d,1], Yanan Jiao[c,e,1], Ruisheng Yang[a,f,1], Yindong Huang[c], Xing Xu[c], Lei Zhang[g,h], Zhaofu Ma[c,e], Ying Yu[d], Wenyu Peng[c], Yifang Yuan[c], Yuan Zhong[c], Songyan Li[e], Yang Yan[e], Fuli Zhang[f], Jiangang Liang[d], Xiaohui Du[e,2], Chao Chang[b,c,2], and Cheng-Wei Qiu[a,i,2]

Edited by David Weitz, Harvard University, Cambridge, MA; received May 27, 2022; accepted September 25, 2022

Optical sensors, with great potential to convert invisible bioanalytical response into readable information, have been envisioned as a powerful platform for biological analysis and early diagnosis of diseases. However, the current extraction of sensing data is basically processed via a series of complicated and time-consuming calibrations between samples and reference, which inevitably introduce extra measurement errors and potentially annihilate small intrinsic responses. Here, we have proposed and experimentally demonstrated a calibration-free sensor for achieving high-precision biosensing detection, based on an optically controlled terahertz (THz) ultrafast metasurface. Photoexcitation of the silicon bridge enables the resonant frequency shifting from 1.385 to 0.825 THz and reaches the maximal phase variation up to 50° at 1.11 THz. The typical environmental measurement errors are completely eliminated in theory by normalizing the Fourier-transformed transmission spectra between ultrashort time delays of 37 ps, resulting in an extremely robust sensing device for monitoring the cancerous process of gastric cells. We believe that our calibration-free sensors with high precision and robust advantages can extend their implementation to study ultrafast biological dynamics and may inspire considerable innovations in the field of medical devices with nondestructive detection.

optical sensors | calibration-free | ultrafast metasurfaces | terahertz | cancer detection

Significance

The premise for developing optical sensors is to guarantee the accurateness and robustness of sensing performance. However, for normalizing signals between samples and reference, the calibration step is always accompanied by environmental noise to undermine the real sensing data. Here, we address this limitation by exploiting an optically controlled terahertz (THz) ultrafast metasurface. The typical measurement errors are completely eliminated through judiciously engineering two transmission spectra between picosecond time delays, to make the sensing calibration-free, high precision, and robust. This work paves an avenue to acquire subtle information and can be extended to series of biosensing applications.

The ability to sense and monitor health condition in human organs is essential to expand our understanding of biological processes for both physiological and pathological pathways (1–3). Biosensors bridging the gap between clinicians and patients can continuously track and transmit biomedical information to support health monitoring and clinical decision making (4–6). For this reason, persistent refinement of biosensors endowing the function to distinguish a specific target from a wide range of samples provides indispensable tools for analytical and biochemical research as well as for medical diagnostics, rehabilitation, and healthcare applications (7–11). Traditional biological detection methods, such as labeled immunoassays, PCR, and light microscopy, still remain important in centralized laboratories when sample volumes are large and an immediate response is not necessary (2). Nevertheless, low-cost, easy-to-use and label-free optical sensors based on biomolecular recognition and measurement of refractive index changes will be a game changer for the diagnosis of diseases, which can be widely used in virtually any location (12–14).

Residing in the frequency domain between the microwave and infrared regions, terahertz (THz) radiation has some peculiar characteristics such as low energy, high resolution, and satisfactory penetration, which renders it a suitable technology for biological studies (15–18). For instance, considering the intramolecular and intermolecular vibrations including hydrogen bonds, van der Waals forces, and nonbonding (hydrophobic) interactions occurring in the THz band, THz technologies naturally open up an additional prospect for the identification of macromolecules like amino acids, proteins, RNA, and DNA (19–21). In addition, the high sensitivity of THz waves to water is perhaps the most exploited research direction in cell biology and has been intensely investigated due to its promising perspectives in cancer detection (22, 23). However, the reported sensors predominantly focus on recognizing the density of cancer cells, while lacking the ability to monitor the evolution process of cells from normal to adenomatous to cancerous states, which is apparently more important in clinical medicine (24–26). Gastric cancer, as the fifth most common cancer and the third most common cause of cancer death worldwide, is diagnosed historically after endoscopic biopsy and staged using computed tomography, endoscopic ultrasound, and laparoscopy (27–29). These methods always detect gastric cancer based on the tumor size and finally diagnose the cancer in a mature state that is already differentiated or is advancing to the late stage. Then treatment can only alleviate suffering but not cure the disease. Thus,

Author contributions: J. Lou, Y.J., R.Y., Y.H., X.X., X.D., and C.-W.Q. designed research; J. Lou, Y.J., X.X., Z.M., Y. Yu, Y. Yuan, S.L., and Y. Yan performed research; J. Lou contributed new reagents/analytic tools; J. Lou, R.Y., L.Z., Y. Yu, W.P., Y. Yuan, Y.Z., F.Z., J. Liang, and C.-W.Q. analyzed data; J. Lou, R.Y., L.Z., C.C., and C.-W.Q. wrote the paper; and X.D., C.C., and C.-W.Q. supervised the project.

The authors declare no competing interest.

This article is a PNAS Direct Submission.

[1]J. Lou, Y.J., and R.Y. contributed equally to this work.

[2]To whom correspondence may be addressed. Email: chengwei.qiu@nus.edu.sg, gwyzlzssb@pku.edu.cn, or duxiaohui301@sina.com.

This article contains supporting information online at http://www.pnas.org/lookup/suppl/doi:10.1073/pnas.2209218119/-/DCSupplemental.

Published October 17, 2022.

to improve the clinical outcome and provide targeted therapy, it is highly desirable to invest in biosensors that can discriminate symptoms at different stages of common gastric cancer, especially that of early cancer.

It is fundamental to strengthen the coupling between analytes and electromagnetic (EM) waves for designing an ultrasensitive optical sensor (4–6). Fortunately, such a demand could be well met via subwavelength meta-atoms in metasurfaces, a flourishing platform for engineering EM waves (30–33). By adjusting the geometry and arrangement pattern of meta-atoms, both the working frequency and the wavefront can be flexibly engineered at will (34, 35). These advances have led to a series of phenomena with an impact on numerous fundamental subjects, such as bioelectronics, imaging, and communications, among others (36–38). To date, much effort has been channeled into releasing metasurfaces and photonic devices for biosensing applications with a high quality factor (Q factor) EM response based on plasmon resonances in metals and Mie resonances in dielectrics (2, 39–41). Despite these achievements, most sensors usually work at a fixed frequency or mode due to the lack of active components or materials, thus hindering the flexibility and practicability of sensing functions. In addition, the existing sensors usually detect the frequency and amplitude change while neglecting the phase data, which may impede the acquisition of unnoticeable biological information. More importantly, ensuring the accurateness and robustness of biosensing performance is the foundation of developing practical sensors, which thus requires the elimination of measurement errors and improvement of signal-to-noise ratio as perfectly as possible. However, the current extraction of biological information for optical sensors is basically processed via a series of complicated and time-consuming calibrations between samples and reference (4, 6, 9), which inevitably introduce extra measurement errors and potentially annihilate small intrinsic responses.

Here, we propose and experimentally demonstrate a calibration-free sensor, by exploiting an optically controlled THz ultrafast metasurface. Based on a homemade optical-pump THz-probe (OPTP) spectroscopy system, an 800-nm pump laser of 2,000 $\mu J/cm^2$ was employed to realize an ultrawide resonant frequency shift from 1.385 to 0.825 THz, as well as a large phase variation up to 50° at 1.11 THz. By normalizing the two measured THz transmission spectra between ultrashort time delays of 37 ps, the typical measurement errors are completely eliminated to realize a high-precision platform for detecting the cancerous evolution of gastric cells. Thus, on the premise of ensuring the accurateness and robustness of biosensing, our proposed calibration-free strategy will pave an additional way to acquire subtle biological information and can be extended to a series of medical applications.

Results

Inspired by the quantum destructive interference between excitation states in atomic physics (42), electromagnetically induced transparency (EIT) has been successfully mimicked in optics via coupling between bright and dark modes (43–45). The transparent and highly dispersive nature of EIT furnishes a feasible solution to the long-standing issue of radiative loss in plasmonic systems. As a result, an EM resonance is obtained with a high Q factor, allowing us to enhance sensing capabilities as well as improve the light–matter interaction strength (43–45). The origin of the EIT mode can be qualitatively described by the coupled Lorentzian oscillator model (44)

$$\begin{aligned} \dot{x}_B - j(\omega_B + j\gamma_B)x_B + jkx_D &= gE_0 e^{j\omega t} \\ \dot{x}_D - j(\omega_D + j\gamma_D)x_D + jkx_B &= 0, \end{aligned} \quad [1]$$

where, (x_B, x_D), (ω_B, ω_D), and (γ_B, γ_D) represent the amplitudes, frequencies, and damping rates of bright and dark modes, respectively; g is the coupling strength of the bright mode to the incident electric field E_0; and k is the coupling coefficient between the bright and dark modes. It is found that the EIT window with an extremely narrow transmission peak could emerge when the bright and dark modes are brought in close proximity in both the spatial and frequency domains. Taking this general principle into consideration, the key issue to equip the metasurfaces with EIT frequency-shifting function is to guarantee a high matching degree between the two modes under different external stimuli (46–52).

Fig. 1*A* demonstrates the schematic illustration of the proposed THz metasurface sensor with a calibration-free property, for monitoring gastric cancers (Fig. 1*B*). Each functional meta-atom consists of two cut wires flanked by a pair of large split-ring resonators (SRRs) and two pairs of small SRRs. A thin layer of patterned epitaxial silicon with a thickness of 600 nm (bandgap of 1.1 eV) is incorporated into the meta-atom as a trigger button. When an external optical laser of 800 nm is shined on the silicon, the free carriers can be pumped from the valence band to the conduction band and an ultrafast shifting of EIT frequency can be achieved. Specifically, without the pump influence, the dipole bright mode of cut wire merely interferes destructively with the inductive capacitive dark mode in the small SRR pair, leading to an EIT response at higher frequency. Once applying a laser pump, the enhanced conductivity of the silicon layer could fuse the two individual cut wires and damp the dark mode of the small SRR pair. In this case, the optically controlled molecularization of discrete dipole resonators via the silicon bridge can be effectively coupled with the large SRR pair and establish a new EIT resonance at lower frequency. Note that the switching speed of the resonant frequency is determined by the dynamics of photogenerated carriers in silicon material.

The geometrical configuration of the optimized meta-atom with detailed structure parameters is presented in Fig. 1*C*, which is composed of three crucial components: bottom sapphire substrate (blue color), middle silicon pattern (red color), and top metallic structure (gold color). To prepare the hybrid metasurfaces, first, we adopted step photolithography and ion beam etching to fabricate a metallic structure on a silicon on sapphire (SOS) substrate. Then, the silicon layer along with the metallic structure was patterned using alignment lithography for mask formation, followed by deep silicon etching to remove the redundant silicon and complete the second graphical transfer. Each of the ultimately prepared metasurfaces has an overall size of 1 × 1 cm^2, ensuring cover of the THz probe spot completely. An optical microscope image of a small portion of the metasurfaces array is shown in Fig. 1*D*. The height distribution of metasurfaces was characterized by atomic force microscopy to verify the high accuracy of sample fabrication (Fig. 1*E*), with Fig. 1 *E*, *Inset* results indicating 165 nm thick metal and 580 nm thick silicon.

To methodically investigate the optical performance of the designed metasurfaces, we first manifested the pump-fluence–controlled active resonances based on a homemade OPTP spectroscopy system (Fig. 2). All measurements were carried out in the nitrogen-filled environment to decrease the absorption of THz waves by water vapor. Under low pump fluences, Fig. 2*A*

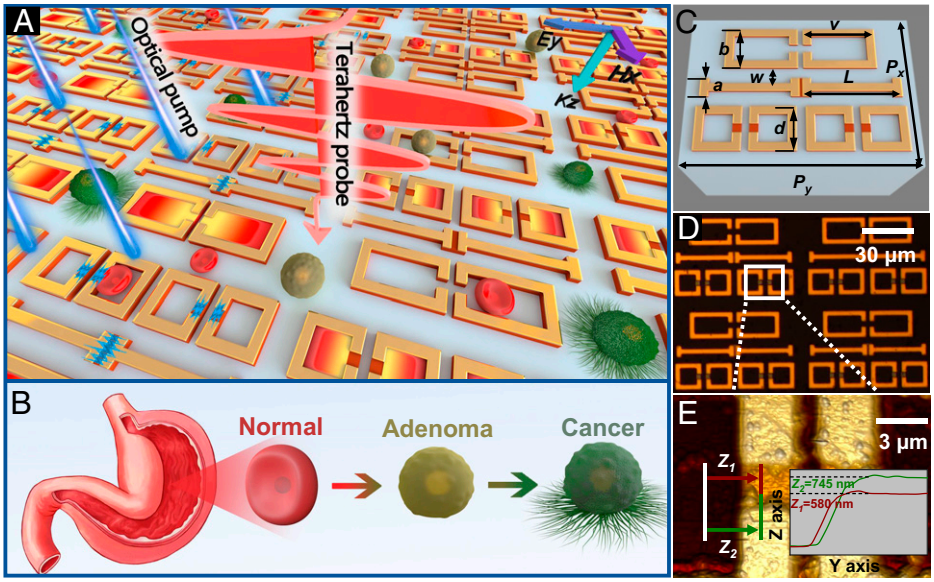

Fig. 1. Design principle and characterization of calibration-free sensors for gastric cancer detection. (*A*) Artistic representation of the hybrid metal–silicon metasurfaces under THz probe and optical excitation implanted by femtosecond laser. The blue lightning inside the silicon bridge implies the excitation of photogenerated carriers. By controlling the pump stimulation, the fiery-red color in different SRR pairs represents the dynamical switching of EIT dark mode and frequency. The THz probe impinges on the metasurfaces at normal incidence (*Kz*) with polarization parallel to the cut wires (*Ey*). (*B*) Cartoon evolution process of gastric cells from normal to adenomatous to cancerous states in clinical medicine. (*C*) Geometrical configuration of the proposed meta-atom within one unit cell with the following structure parameters: P_x = 56 μm, P_y = 80 μm, L = 34.5 μm, a = 7 μm, w = 5.6 μm, d = 15.8 μm, b = 16 μm, and v = 26 μm. The gap width of the silicon bridge in cut wires and small SRRs is 1 and 3 μm, respectively. (*D*) An optical microscope image of the fabricated metasurfaces. (*E*) An atomic force microscopy image of part of a small SRR pair to characterize the height of the silicon bridge (580 nm) and metal structure (165 nm).

presents the original transmission amplitude of the metasurfaces ranging from 0.5 to 2.0 THz, after basic Fourier transformation. It is clearly observed that the EIT peak at 1.385 THz (denoted as EIT_I) undergoes a strong modulation as the pump fluence increases, whereas the other frequency band stays almost unchanged. When the pump fluence is set at 50 μJ/cm^2, the EIT_I window is completely switched off, indicating 100% modulation depth. Next, different from traditional calibration

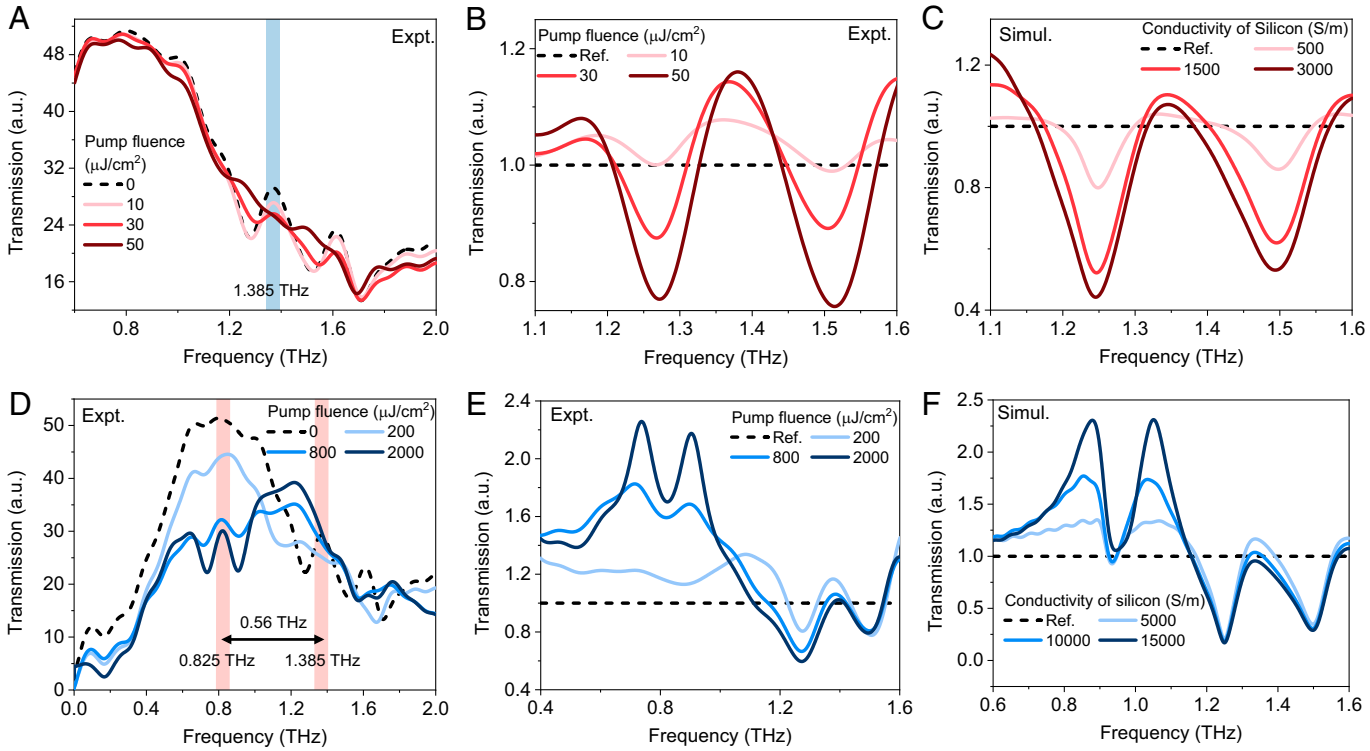

Fig. 2. Pump-fluence–controlled EIT response of the metasurfaces based on an OPTP system. (*A* and *B*) Experimentally (*A*) original and (*B*) normalized THz transmission under low pump fluences from 0 to 25 μJ/cm^2. The black dashed line in *A* corresponds to the reference line in *B*. (*C*) Corresponding simulated transmission of THz metasurfaces with lower conductivities of silicon from 0 to 3,000 S/m. (*D* and *E*) Experimentally (*D*) original and (*E*) normalized THz transmission under high pump fluences from 0 to 2,000 μJ/cm^2. (*F*) Corresponding simulated results of THz metasurfaces with higher conductivities of silicon from 0 to 15,000 S/m.

methods (46–52), the transmission amplitude and phase spectra are obtained by redefining the normalized formula

$$|\tilde{t}(\omega)| = E_R(\omega)/E_P(\omega)$$
$$\varphi(\omega) = \varphi_R(\omega) - \varphi_P(\omega), \quad [2]$$

where $[E_R(\omega), E_P(\omega)]$, $[\varphi_R(\omega), \varphi_P(\omega)]$ are the Fourier amplitudes and phases passing through the metasurfaces under 0 and varying pump fluences, respectively.

As THz waves propagate through the air, it would interact with water vapor, resulting in the superimposition of water vapor noise on the sample signal in both time and frequency domains. In some cases where accurate measurements are needed, the water vapor noise could lead to unavoidable measurement errors, which probably annihilate weak but essential information.

Supposing a sample with a thickness d and a total propagating distance $\Delta L + d$, the sample signal carrying the water vapor noise is mathematically expressed as (53)

$$E(\nu)_{\text{sam+vapor}} = E(\nu)_{\text{nitrogen}}\, t_{as}t_{sa}\exp\left(\frac{-j2\pi\nu\tilde{n}_s(\nu)d}{c}\right) \times \exp\left\{\frac{\Delta L\alpha(\nu)}{2}\right\}\exp\left\{\frac{-j2\Delta L\pi\nu n(\nu)}{c}\right\}, \quad [3]$$

where t_{as} and t_{sa} are the transmission coefficients from air to sample surface and from sample to air surface, respectively; $\tilde{n}_s(\nu)$ is the effective refractive index of the sample; and $\alpha(\nu)$ and $n(\nu)$ represent absorption coefficient and refractive index of water vapor, respectively. For the traditional calibration method (*SI Appendix*, Note 1), the typical measurement error is enhanced significantly with air humidity and sample thickness:

$$W(\nu)_{\text{erro}} = \exp\left\{-\frac{d\alpha(\nu)}{2}\right\}\exp\left\{\frac{j2d\pi\nu n(\nu)}{c}\right\}. \quad [4]$$

Impressively, this error can be eliminated through dividing the ultrafast laser pumping signal by the original signal under the no pumping condition, which leads to an accurate calibration-free method. When the laser pump is applied, the electric-field vector of the transmission signal is

$$E(\nu)'_{\text{sam+vapor}} = E(\nu)_{\text{nitrogen}}\, t'_{as}t'_{sa}\exp\left(\frac{-j2\pi\nu\tilde{n}'_s(\nu)d}{c}\right) \times \exp\left\{\frac{\Delta L\alpha(\nu)}{2}\right\}\exp\left\{\frac{-j2\Delta L\pi\nu n(\nu)}{c}\right\}. \quad [5]$$

And the target sample signal is normalized as

$$E(\nu)_{\text{sc}} = E(\nu)_{\text{sam+vapor}}/E'(\nu)_{\text{sam+vapor}} \quad [6]$$

$$E(\nu)_{\text{sc}} = \frac{t_{as}t_{sa}}{t'_{as}t'_{sa}}\exp\left(\frac{-j2\pi\nu[\tilde{n}_s(\nu) - \tilde{n}'_s(\nu)]d}{c}\right). \quad [7]$$

From Eq. 7, it is found that the water vapor noise has completely disappeared using this method.

Based on Eq. **2**, the black dashed line in Fig. 2*A* (in the absence of optical excitation) corresponds to the reference line in Fig. 2*B* (reference: $\tilde{t}(\omega) = 1$). Interestingly, in contrast to the annihilation of the EIT_I window in the original data, it is found that the EIT_I peak in the normalized form becomes enhanced as the pump fluence increases (Fig. 2*B*). To verify the rationality of EIT_I modulation theoretically, we performed numerical simulation using CST Microwave Studio Software in the time domain. In the simulation, the dielectric constants of sapphire and silicon are 9.3 and 11.9, respectively. The direct current conductivity of gold is 4.56×10^7 S/m. The simulated transmission spectra under various conductivities of silicon from 0 to 3,000 S/m match well with the experimental results, as shown in Fig. 2*C*. The underlying physical mechanism of EIT_I modulation can be unveiled by the field distributions at 1.385 THz (*SI Appendix*, Fig. S2).

As aforementioned, further enhancing the conductivity of silicon would eliminate the physical isolation of the two cut wires and build a new EIT window at lower frequency. Fig. 2*D* demonstrates the original Fourier transmission amplitude under high pump fluences, from which we can see that the frequency of the EIT peak shifts from 1.385 to 0.825 THz with an extremely large tuning range up to 40.4%. The origin of the EIT frequency-shifting function is particularly clarified in *SI Appendix*, Fig. S2. By employing the calibration-free method, we obtain the normalized transmission spectra of the metasurfaces (Fig. 2*E*). One can see that the inverted EIT window at 0.825 THz (denoted as EIT_{II}) is reinforced with increasing pump fluences, while the initial EIT_I window is generally well preserved in outline. As the pump fluence increases up to 2,000 μJ/cm^2, the transmission spectrum exhibits an approximately diagonal-symmetry profile with a dual-EIT window (dark blue line in Fig. 2*E*). Additionally, the numerical simulation with high conductivities of silicon from 0 to 15,000 S/m is presented in Fig. 2*F*, which displays a similar trend to the experimental results.

In view of the ultrafast charge-carrier dynamics in silicon, another intriguing phenomenon deserving to be explored is the transient evolution process of THz transmission of the silicon-based metasurfaces, upon femtosecond pump illumination. The free-carrier relaxation dynamics for the 600-nm-thick silicon layer are revealed by recording the transient modulation of the THz pulse ($-\Delta E/E_0$), together with the extracted fluence-dependent photoconductivity shown in *SI Appendix*, Fig. S1. The pump–probe time delay represents the relative time difference between the arrival of the optical pump and the THz pulse at the sample, which can be controlled by translational stages. The time delay of 0 ps is identified as the inception point for carrier excitation.

Under a fixed pump fluence of 2,000 μJ/cm^2, the THz transmission amplitude and phase at different frequencies are plotted as a function of pump–probe time delay from −4.5 to 36 ps (Fig. 3 *A* and *B*). The upper and lower red dashed lines denote the frequency of EIT_I peak and EIT_{II} dip, respectively. As visualized in Fig. 3*A*, the transmission amplitude of the THz metasurfaces remains around 1 before the pump pulse is injected into the silicon bridge. Once the femtosecond laser impinges on the sample after 0 ps, photogenerated carriers immediately help to construct the preliminary outline of the EIT_I window located at 1.385 THz. With the accumulation of more free carriers, the EIT_{II} window at 0.825 THz begins to emerge at 27 ps, and then the overall transmission amplitude gradually tends to be stable. The 27 ps of the evolution process from EIT_I to EIT_{II} can be attributed to the step-like behavior of carrier excitation (*SI Appendix*, Fig. S3). Similar to the amplitude modulation, the phase variation of the metasurfaces also exhibits a transient evolution property at above two critical time points (Fig. 3*B*). Originating from the ultrawide frequency shifting (0.56 THz) of coupled-harmonic oscillations, it is observed that the giant modulation of transmission phase occurs in the frequency domain between the two EIT resonances and the maximal phase variation reaches as high as 50°. We extract the amplitude and phase spectra from the corresponding contour maps at several pump–probe time delays

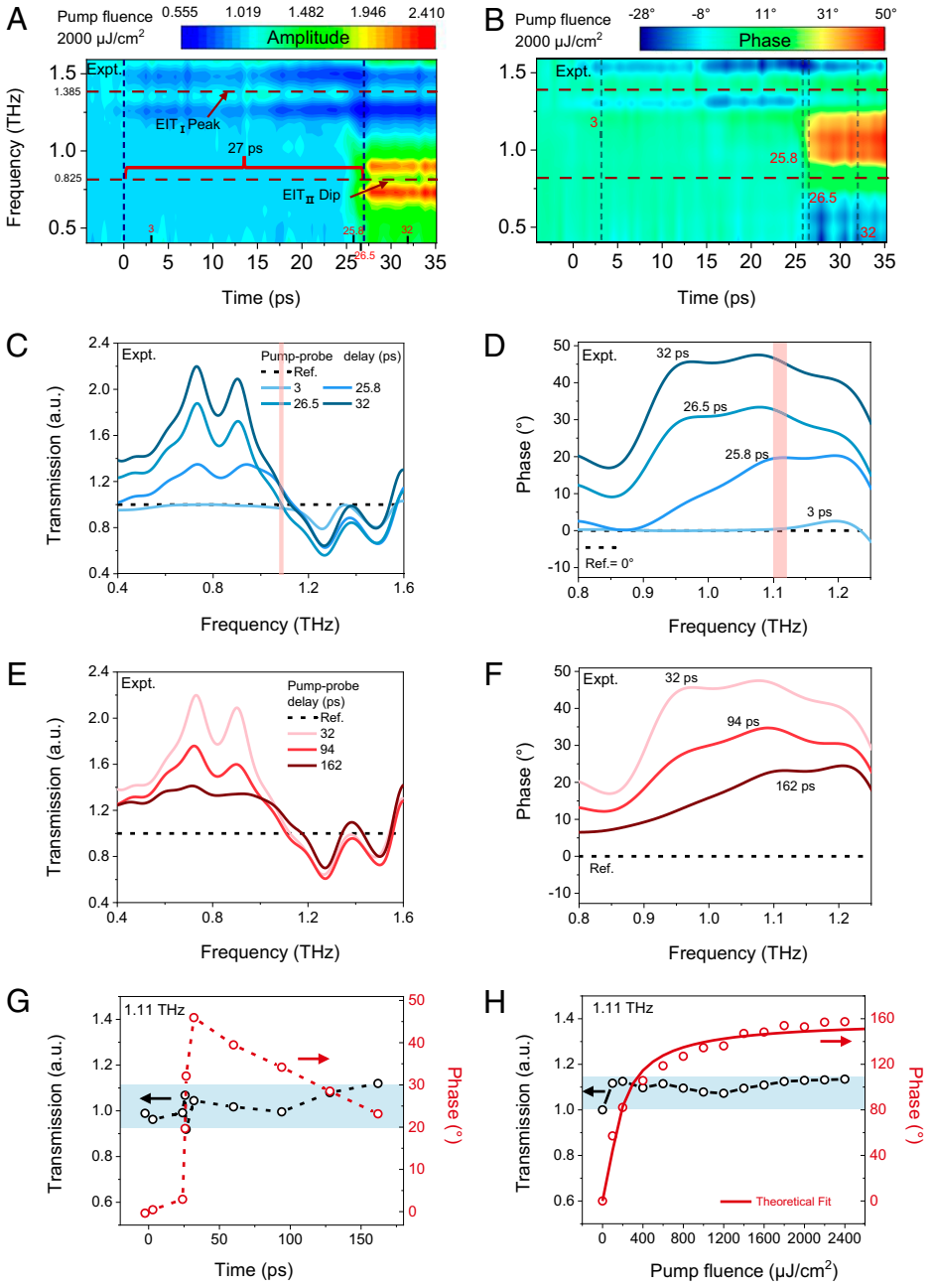

Fig. 3. Transient evolution process of the ultrafast EIT frequency-shifting metasurfaces. (*A* and *B*) Experimental transmission (*A*) amplitude and (*B*) phase contour color maps for the metasurfaces against pump–probe time delay, under a fixed pump fluence of 2,000 μJ/cm^2. (*C* and *D*) Experimental THz-normalized (*C*) amplitude and (*D*) phase spectra at various pump–probe time delays from 3 to 32 ps, extracted from the corresponding contour maps. (*E* and *F*) Experimental THz-normalized (*E*) amplitude and (*F*) phase spectra at various pump–probe time delays from 32 to 162 ps. (*G*) Experimentally extracted amplitude and phase results for the THz metasurfaces versus pump–probe time delay at 1.11 THz. (*H*) Experimentally extracted amplitude and phase results for the THz metasurfaces against pump fluence at 1.11 THz. The fitting solid line indicates a single exponential function.

(Fig. 3 *C* and *D*), to explicitly demonstrate the switching-on course of the dual-EIT spectrum. During the time span from 0 to 32 ps, the dual-EIT transmission profile is gradually constructed with an enhanced resonant strength (Fig. 3*C*). For the phase spectra in Fig. 3*D*, the phase variation ranging from 0 to more than 45° is realized by recognizing the differences between lines of reference and 32 ps. Moreover, the transmission results residing in 1.1 to 1.12 THz (light red areas in Fig. 3 *C* and *D*) are highlighted in *SI Appendix*, Fig. S5. For the switching-off course, the amplitude and phase spectra of metasurfaces in the case of several pump–probe time delays are recorded in Fig. 3 *E* and *F*. It is seen that the annihilation of the EIT_{II} window is significant, while the EIT_I changes slightly as the time delay increases (Fig. 3*E*), which is limited by the maximum moving distance of translational stages. In sync with the amplitude modulation, the phase spectrum is also not fully recovered to the reference line until 162 ps (Fig. 3*F*), which can be attributed to the relaxation features of the epitaxial silicon film (43, 45). The amplitude and phase spectra can restore to their initial states within a timescale of nanoseconds.

By quantitively analyzing the transmission results at 1.11 THz (Fig. 3*G*), the middle frequency of two EIT resonances, it is worth emphasizing that the phase variation of the metasurfaces also exhibits a time-resolved property related to the ultrafast dynamics of silicon-free carriers (*SI Appendix*, Fig. S1*A*), while the amplitude merely fluctuates in the 13.9% range. Furthermore, upon varying

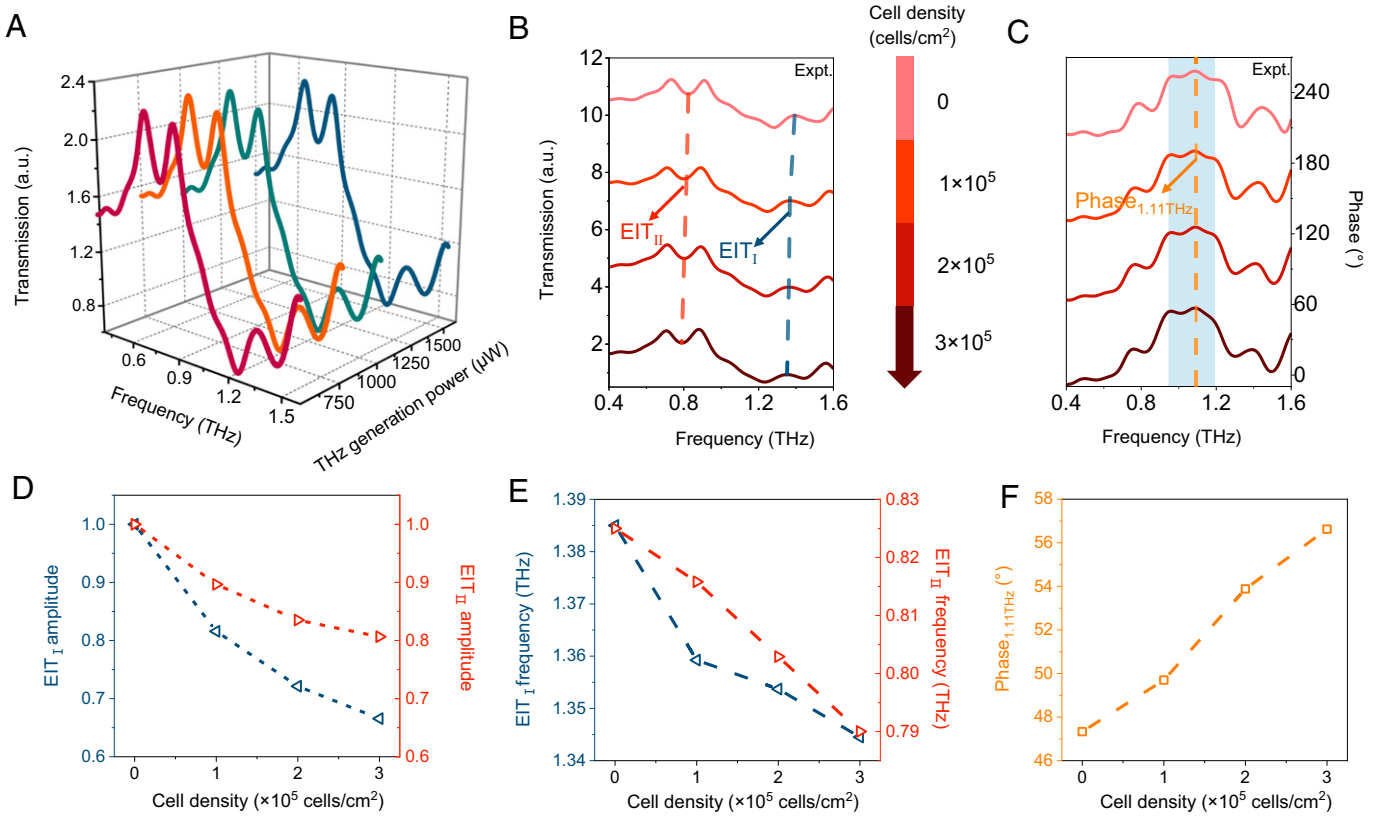

Fig. 4. Measured biosensing performance for the calibration-free sensors. (*A*) Experimentally normalized THz amplitude spectra with varying THz generation power. (*B* and *C*) Experimental THz transmission (*B*) amplitude and (*C*) phase spectra against cell densities of GCCs. (*D* and *E*) Extracted (*D*) relative amplitudes and (*E*) frequencies of EIT resonances versus different cell densities of GCCs. (*F*) Extracted phase$_{1.11\text{THz}}$ versus different cell densities of GCCs.

pump fluences from 0 to 2,400 μJ/cm^2, we summarize the tuning trend of transmission amplitude and phase at 1.11 THz, from which one can observe that the modulation in amplitude is suppressed below 11.8% (black line in Fig. 3*H*). The phase at 1.11 THz exponentially increases with pump fluence (red line in Fig. 3*H*), which is associated with the optically induced conductivity variation of silicon (*SI Appendix*, Fig. S1*B*). Consequently, benefitting from the well-performed regularity and sensitivity, the transmission phase naturally provides us with another sensing aspect, in addition to the conventional frequency and amplitude. Moreover, by combining with the advantages of large phase variation and high amplitude stability, our proposed metasurface could also act as an outstanding candidate for a series of active optical encoding applications (34), such as meta-antennas, meta-holograms, metalenses, etc.

To explore the biosensing behaviors, it is necessary to evaluate the accurateness and robustness of calibration-free methods first, which is essential to guarantee the reliability of experimental data. By altering THz generation power, we measured four pairs of transmission results in both time and frequency domains under a fixed pump fluence of 2,000 μJ/cm^2 (*SI Appendix*, Fig. S6) and obtained the corresponding normalized amplitude spectra shown in Fig. 4*A*. The visualized amplitude, phase, and resonant frequencies of the four spectra are almost identical to each other, with the concrete error analysis shown in Table 1. The comparison of measurement errors between calibration-free and substrate calibration methods can be seen in *SI Appendix*, Note 7.

Next, the practical performances for THz biosensing were carried out by culturing the human normal gastric epithelial cells (NGECs), gastric adenoma cells (GACs), and gastric cancer cells (GCCs) onto the surface of the metasurfaces. The types of NGECs, GACs, and GCCs are GES-1, intestinal-type adenoma (MUC2+, CD10+), and MGC-803, respectively. The time-dependent growth curves of the three types of gastric cells planted in the culture medium are demonstrated in *SI Appendix*, Fig. S9. Note that the cell density tends to be saturated after a rapid exponential growth. Upon a fixed pump fluence of 2,000 μJ/cm^2, we obtained several pairs of THz transmission results at pump–probe time delays of −5 and 32 ps, respectively. The normalized transmission amplitude and phase spectra of the metasurface sensors covered by GCCs with varying cell densities from 0 to 3 × 10^5 cells/cm^2 are displayed in Fig. 4 *B* and *C*. As the cell density increases, both the two EIT resonant frequencies show redshift (dashed lines in Fig. 4*B*), along with a phase increment occurring around 1.1 THz (blue area in Fig. 4*C*). Assume that the GCCs are covered on the metasurfaces as a homogeneous dielectric layer with fixed thickness, where the nucleus mainly

Table 1. Error analysis based on calibration-free method

	EIT amplitude, a.u.	EIT$_\text{I}$ frequency, THz	EIT$_\text{II}$ frequency, THz	Phase at 1.11 THz, °
Average value	1.332	1.385	0.825	47.33
SD	0.009	0.0007	0.002	0.3347

determines the dielectric constant ε_{cell}, while the conductivity σ_{cell} mainly depends on the water content inside the cell fluid, according to the basic configuration of gastric cells. Thus, both the two factors ε_{cell} and σ_{cell} are positively correlated with the cell density. We also calculate the phase spectra with different ε_{cell} and σ_{cell} to illustrate how the optical property of the dielectric layer influences the phase variation (*SI Appendix*, Fig. S11). To obtain a deeper insight into the sensing effect, we extract relative amplitudes and resonant frequencies of EIT_I and EIT_{II} against cell density of GCCs (Fig. 4 *D* and *E*), respectively. It is noted that both the amplitudes and frequencies of EIT_I and EIT_{II} decrease with the increase of cell density, which is because both ε_{cell} and σ_{cell} of the dielectric layer increase with the total of nucleus and cell fluid, respectively. Considering that the phase variation (blue area in Fig. 4*C*) is almost linearly related with the cell density of GCCs, we also extract the transmission phase at 1.11 THz ($phase_{1.11THz}$) under different cell densities from 0 to 3×10^5 cells/cm^2 (Fig. 4*F*). It is observed that the $phase_{1.11THz}$ exhibits an $\sim 3.0978°/10^5$ cells·cm^{-2} linear relationship with cell density, indicating that our metasurface can be employed as a promising platform for sensitive detections.

For monitoring the cancerous process of gastric cells, we obtain the absolute change of EIT_I frequency (ΔF), EIT_I amplitude (ΔA), and $phase_{1.11THz}$ (ΔP) with cell densities from 0 to 3×10^5 cells/cm^2 of GCCs, GACs, and NGECs, respectively (Fig. 5 *A*–*C*). All three key sensing factors exhibit an increasing trend with larger cell density. In terms of ΔF and ΔA, the slope corresponding to NEGCs is larger than that of GACs and that of GCCs, for the reason that the net sizes of nucleus and cell fluid become smaller with the cells changing from normal to adenomatous to cancerous states. Thus, both the ε_{cell} and σ_{cell} of the dielectric layer become smaller in this cancerous process, leading to the reductions of ΔF and ΔA. Fig. 5*C* shows the ΔP versus different cell densities of GCCs, GACs, and NGECs, where the slope corresponding to NEGCs is smaller than that of GACs and that of GCCs, corresponding to 1.4947°, 2.316°, and $3.0978°/10^5$ cells·cm^{-2}, respectively. The slope order of ΔP displays the opposite trend to ΔF and ΔA for the three types of gastric cells. This is because the ratio of nucleus to cell fluid gradually increases within the evolution of gastric cancers. Specifically, the phase variation increases with larger ε_{cell} for nucleus, while it exhibits a downward trend with larger σ_{cell} for cell fluid. Although the nucleus and cell fluid of gastric cells together reduce within the cancerous process of gastric cells, while the relative ratio of nucleus to cell fluid increases, thus resulting in a faster change of ΔP for GCCs. Besides, considering the adopted optical excitation as a femtosecond pump, the influence of the 2-mJ/cm^2 laser on gastric cells is discussed in *SI Appendix*, Note 11.

We also conducted cell-staining experiments to confirm these findings (Fig. 5 *D*–*F*). The cell dye in our experiments is hematoxylin. The light gray and dark areas represent cell and nucleus outlines (black and red dashed lines in Fig. 5*D*), respectively. It is observed that within the cancerous process of gastric cells, the absolute net sizes of cell and nucleus decrease gradually while the ratio of nucleus to cell fluid shows an increasing trend, which is consistent with the THz-biosensing results.

Conclusion

To eliminate the typical measurement errors caused by the traditional calibration method, we demonstrate a class of calibration-free sensors to leverage a high-precision and robust platform for biosensing detections, based on optically controlled THz ultrafast

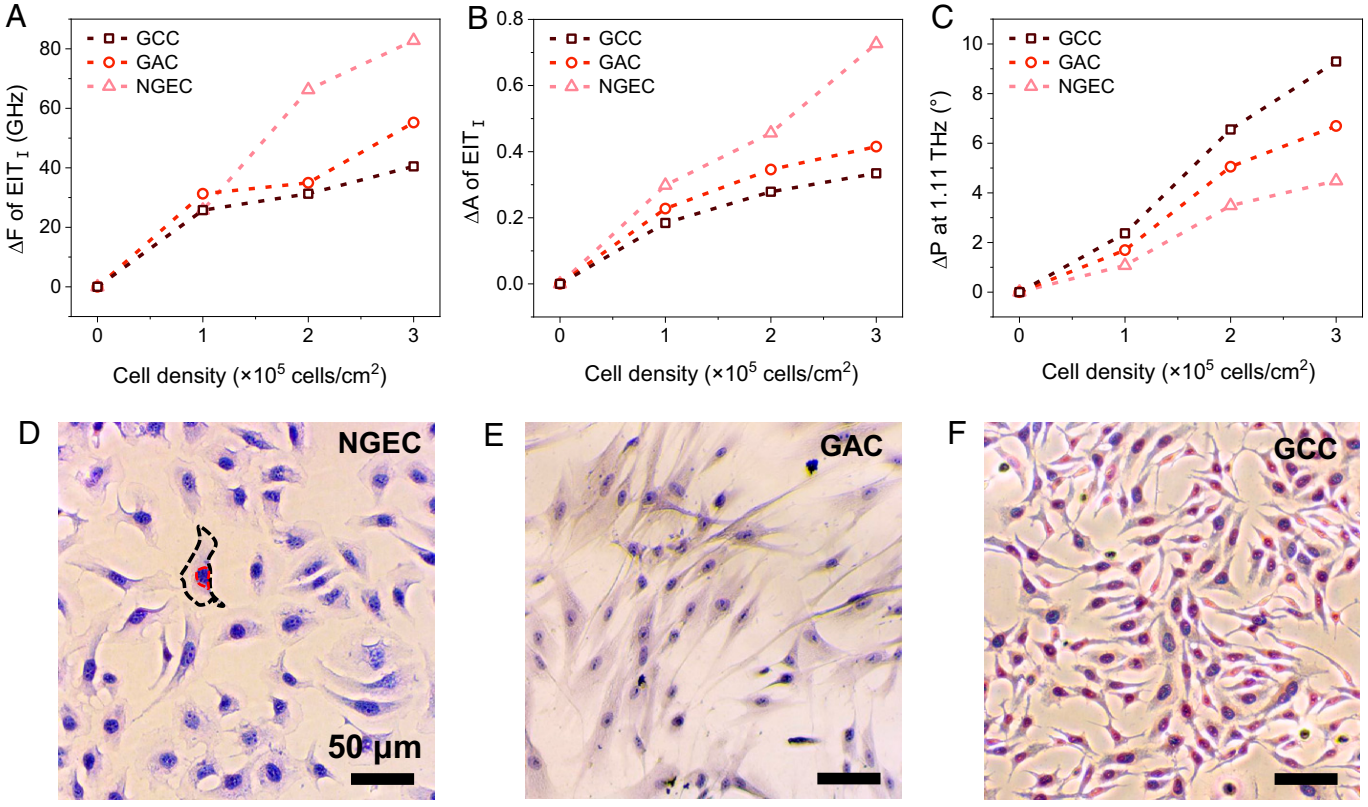

Fig. 5. Monitoring the cancerous evolution of gastric cells. (*A*–*C*) Extracted absolute change of (*A*) EIT_I frequency, (*B*) EIT_I amplitude, and (*C*) $phase_{1.11THz}$ against cell densities of three gastric cells. (*D*–*F*) Cell staining results for (*D*) NGECs, (*E*) GACs, and (*F*) GCCs. The black and red dashed lines (*D*) illustrate cell and nucleus outlines, respectively.

metasurfaces. An optical pump of 800 nm enables the excitation of silicon carriers to shift resonant frequency from 1.385 to 0.825 THz, accompanied by a large phase variation up to 50° at 1.11 THz. By normalizing the transmission results with two hugely different THz spectra between ultrashort time delays of 37 ps, the environment noise along the THz propagation path is completely removed to guarantee the reliability of biosensing results. The calibration-free transmission spectra have successfully discriminated the categories of gastric cells, which is consistent with the cell-staining experiments. Thus, we anticipate that our calibration-free biosensing method will inspire many more medical applications and open up previously unnoticed horizons for biosensing applications in THz and infrared domains.

Materials and Methods

Sample Preparation. The fabrication of THz metasurfaces functioning with ultrafast EIT frequency-shifting ability was processed based on lithography and etching technologies. First, we selected a 4-inch SOS wafer consisting of a 460-μm-thick sapphire and 600-nm-thick epitaxial silicon layer as the substrate. According to the manufacturer, the front surface of the SOS wafer was Epi-polished with Ra $\leq$ 0.3 nm and the back surface was optically polished. The intrinsic resistivity of the single crystalline (001) silicon layer was >100 Ω/cm. Second, step lithography and ion beam etching were adopted to achieve the first graphical transfer on the metal thin film, followed by depositing 10-nm-thick titanium and 160-nm-thick gold using Radio-frequency (RF) magnetron sputtering. After the cleaning process in acetone and isopropyl alcohol, the silicon pattern along with the metallic structure was defined again by positive photoresist based on alignment lithography. Then, the deep silicon etching technology was carried out to remove the redundant silicon and complete the second graphical transfer. The etching accuracy along the lateral and longitudinal directions is ±0.3 μm and +3.3%, respectively. Finally, by means of slicing technology, the 4-inch sample was divided into several 1 × 1-cm^2 individual metasurfaces, containing 22,321 functional meta-atoms.

Cell Culture. The human gastric mucosal epithelial cells, gastric adenoma cells, and cancer cells acquired from the Institute of General Surgery of the Chinese People's Liberation Army General Hospital were first cultured in a 37 °C humidified incubator with 5% CO_2. Three kinds of gastric cells were all deidentified prior to use in our study. Then, three cells were planted on the 1 × 1-cm^2 THz metasurfaces (the initial concentration was fixed at 4 × 10^4 cells/cm^2) and cultured in complete medium containing RPMI-1640 medium (Thermo), 10% fetal bovine serum (FBS), 1% Glutamax (Gibco), and 0.2% plasmocin prophylactic (InvivoGen). After that, the number of cells was counted by Cell Count (Thermo; CountessIII) at specific time points to obtain the characteristics of the proliferation of cells on the THz metasurfaces. According to the growth curves of the three cells (*SI Appendix*, Fig. S9), specific cell densities of 1 × 10^5, 2 × 10^5, and 3 × 10^5 cells/cm^2 were selected to test the biosensing performance of the calibration-free metasurfaces (*SI Appendix*, Fig. S10).

THz Transmission Measurement. In the homemade OPTP system (*SI Appendix*, Fig. S14), the laser source was a Ti: sapphire laser amplifier with 800 nm central wavelength, 100 fs pulse duration and 1 kHz repetition rate. Each output laser pulse with 5 mJ energy was divided into three beams, for THz generation, detection, and sample excitation, respectively. First, the THz emission was generated from the two-color laser-induced gas plasma, by utilizing a 100-μm-thick β-barium borate crystal and a plano-convex lens of 30 cm focal length. Second, the transmitted THz wave was detected through the technique of electro-optic sampling (EOS) with a 2-mm-thick ZnTe crystal. Third, the excitation laser beam (optical pump) and the THz wave (THz probe) acted together on the sample surface. To ensure uniform photoexcitation, the spot size of the optical pump beam (~8 mm diameter) was larger than the THz probe beam spot (~4 mm diameter). The pump–probe time delay was controlled by moving the translational stage to change the optical path of the pump beam. Finally, the modulated THz waveform was recorded by the EOS technique, and the corresponding THz transmission result was obtained by a standard Fourier transform. To eliminate the influences of surface analytes on photogenerated carriers, the THz probe and optical pump are together incident from the backside of the sample during the measurement.

Data, Materials, and Software Availability. All study data are included in the article and/or *SI Appendix*.

ACKNOWLEDGMENTS. We acknowledge the support from the National Natural Science Foundation of China (Grants 61731010, 11874142, and T2241002). C.-W.Q. acknowledges the support from Grant A-0005947-02-00 from the Advanced Research and Technology Innovation Centre at National University of Singapore. C.C. acknowledges the support from the XPLORER PRIZE (2020-1023). R.Y. acknowledges the support from the China Scholarship Council (Grant 202106290086).

Author affiliations: [a]Department of Electrical and Computer Engineering, National University of Singapore, 117583 Singapore, Singapore; [b]School of Physics, Peking University, 100871 Beijing, China; [c]Innovation Laboratory of Terahertz Biophysics, National Innovation Institute of Defense Technology, 100071 Beijing, China; [d]Air and Missile Defense College, Air Force Engineering University, 710051 Xi'an, China; [e]Department of General Surgery, First Medical Center, Chinese People's Liberation Army (PLA) General Hospital, 100853 Beijing, China; [f]School of Physical Science and Technology, Northwestern Polytechnical University, Xi'an, China; [g]Key Laboratory for Physical Electronics and Devices of the Ministry of Education, School of Electronic Science and Engineering, Xi'an Jiaotong University, 710049 Xi'an, China; [h]Shanxi Key Laboratory of Information Photonic Technique, School of Electronic Science and Engineering, Xi'an Jiaotong University, 710049 Xi'an, China; and [i]National University of Singapore (NUS) Suzhou Research Institute, Suzhou Industrial Park, 215123 Suzhou, China

1. R. Li *et al.*, A body map of somatic mutagenesis in morphologically normal human tissues. *Nature* **597**, 398–403 (2021).
2. H. Altug, S. H. Oh, S. A. Maier, J. Homola, Advances and applications of nanophotonic biosensors. *Nat. Nanotechnol.* **17**, 5–16 (2022).
3. S. K. Elledge *et al.*, Engineering luminescent biosensors for point-of-care SARS-CoV-2 antibody detection. *Nat. Biotechnol.* **39**, 928–935 (2021).
4. A. John-Herpin, D. Kavungal, L. von Mücke, H. Altug, Infrared metasurface augmented by deep learning for monitoring dynamics between all major classes of biomolecules. *Adv. Mater.* **33**, e2006054 (2021).
5. A. Hassibi *et al.*, Multiplexed identification, quantification and genotyping of infectious agents using a semiconductor biochip. *Nat. Biotechnol.* **36**, 738–745 (2018).
6. A. Tittl *et al.*, Imaging-based molecular barcoding with pixelated dielectric metasurfaces. *Science* **360**, 1105–1109 (2018).
7. A. Quijano-Rubio *et al.*, De novo design of modular and tunable protein biosensors. *Nature* **591**, 482–487 (2021).
8. F. J. Sánchez-Rivera *et al.*, Base editing sensor libraries for high-throughput engineering and functional analysis of cancer-associated single nucleotide variants. *Nat. Biotechnol.* **40**, 862–873 (2022).
9. F. Yesilkoy *et al.*, Ultrasensitive hyperspectral imaging and biodetection enabled by dielectric metasurfaces. *Nat. Photonics* **13**, 390 (2019).
10. M. D. Baaske, M. R. Foreman, F. Vollmer, Single-molecule nucleic acid interactions monitored on a label-free microcavity biosensor platform. *Nat. Nanotechnol.* **9**, 933–939 (2014).
11. J. Kim, A. S. Campbell, B. E. de Ávila, J. Wang, Wearable biosensors for healthcare monitoring. *Nat. Biotechnol.* **37**, 389–406 (2019).
12. M. U. Ahmed, I. Saaem, P. C. Wu, A. S. Brown, Personalized diagnostics and biosensors: A review of the biology and technology needed for personalized medicine. *Crit. Rev. Biotechnol.* **34**, 180–196 (2014).
13. S. Shrivastava, T. Q. Trung, N.-E. Lee, Recent progress, challenges, and prospects of fully integrated mobile and wearable point-of-care testing systems for self-testing. *Chem. Soc. Rev.* **49**, 1812–1866 (2020).
14. S. Jain *et al.*, Internet of medical things (IoMT)-integrated biosensors for point-of-care testing of infectious diseases. *Biosens. Bioelectron.* **179**, 113074 (2021).
15. B. Ferguson, X.-C. Zhang, Materials for terahertz science and technology. *Nat. Mater.* **1**, 26–33 (2002).
16. K. Sengupta, T. Nagatsuma, D. M. Mittleman, Terahertz integrated electronic and hybrid electronic–photonic systems. *Nat. Electron.* **1**, 622 (2018).
17. A. G. Davies, A. D. Burnett, W. Fan, E. H. Linfield, J. E. Cunningham, Terahertz spectroscopy of explosives and drugs. *Mater. Today* **11**, 18 (2008).
18. A. Markelz, S. Whitmire, J. Hillebrecht, R. Birge, THz time domain spectroscopy of biomolecular conformational modes. *Phys. Med. Biol.* **47**, 3797–3805 (2002).
19. X. Yang, K. Yang, Y. Luo, W. Fu, Terahertz spectroscopy for bacterial detection: Opportunities and challenges. *Appl. Microbiol. Biotechnol.* **100**, 5289–5299 (2016).
20. M. Beruete, I. Jáuregui-López, Terahertz sensing based on metasurfaces. *Adv. Opt. Mater.* **8**, 1900721 (2019).
21. B. Fischer *et al.*, Terahertz time-domain spectroscopy and imaging of artificial RNA. *Opt. Express* **13**, 5205–5215 (2005).
22. E. Pickwell *et al.*, Simulating the response of terahertz radiation to basal cell carcinoma using ex vivo spectroscopy measurements. *J. Biomed. Opt.* **10**, 064021 (2005).
23. X. Yan *et al.*, The terahertz electromagnetically induced transparency-like metamaterials for sensitive biosensors in the detection of cancer cells. *Biosens. Bioelectron.* **126**, 485–492 (2019).
24. Y. Wu *et al.*, Identification of microbial markers across populations in early detection of colorectal cancer. *Nat. Commun.* **12**, 3063 (2021).

25. D. Calebiro *et al.*, PKA catalytic subunit mutations in adrenocortical Cushing's adenoma impair association with the regulatory subunit. *Nat. Commun.* **5**, 5680 (2014).
26. I. Soncin *et al.*, The tumour microenvironment creates a niche for the self-renewal of tumour-promoting macrophages in colon adenoma. *Nat. Commun.* **9**, 582 (2018).
27. E. C. Smyth, M. Nilsson, H. I. Grabsch, N. C. van Grieken, F. Lordick, Gastric cancer. *Lancet* **396**, 635–648 (2020).
28. F. Bray *et al.*, Global cancer statistics 2018: GLOBOCAN estimates of incidence and mortality worldwide for 36 cancers in 185 countries. *CA Cancer J. Clin.* **68**, 394–424 (2018).
29. I. J. Choi *et al.*, Family history of gastric cancer and *Helicobacter pylori* treatment. *N. Engl. J. Med.* **382**, 427–436 (2020).
30. S. Rajabali *et al.*, Polaritonic nonlocality in light–matter interaction. *Nat. Photonics* **15**, 690 (2021).
31. D. Rodrigo *et al.*, APPLIED PHYSICS. Mid-infrared plasmonic biosensing with graphene. *Science* **349**, 165–168 (2015).
32. C. Wu *et al.*, Fano-resonant asymmetric metamaterials for ultrasensitive spectroscopy and identification of molecular monolayers. *Nat. Mater.* **11**, 69–75 (2011).
33. Y. Zhu *et al.*, Optical conductivity-based ultrasensitive mid-infrared biosensing on a hybrid metasurface. *Light Sci. Appl.* **7**, 67 (2018).
34. N. Shitrit *et al.*, Spin-optical metamaterial route to spin-controlled photonics. *Science* **340**, 724–726 (2013).
35. H. Sroor *et al.*, High-purity orbital angular momentum states from a visible metasurface laser. *Nat. Photonics* **14**, 498 (2020).
36. L. Li *et al.*, Electromagnetic reprogrammable coding-metasurface holograms. *Nat. Commun.* **8**, 197 (2017).
37. G. Hu *et al.*, Coherent steering of nonlinear chiral valley photons with a synthetic Au–WS2 metasurface. *Nat. Photonics* **13**, 467 (2019).
38. Z. Li, X. Tian, C. W. Qiu, J. S. Ho, Metasurfaces for bioelectronics and healthcare. *Nat. Electron.* **4**, 382 (2021).
39. A. Ahmadivand, B. Gerislioglu, R. Ahuja, Y. K. Mishra, Terahertz plasmonics: The rise of toroidal metadevices towards immunobiosensings. *Mater. Today* **32**, 108 (2020).
40. M. Lawrence *et al.*, High quality factor phase gradient metasurfaces. *Nat. Nanotechnol.* **15**, 956–961 (2020).
41. D. Rodrigo *et al.*, Resolving molecule-specific information in dynamic lipid membrane processes with multi-resonant infrared metasurfaces. *Nat. Commun.* **9**, 2160 (2018).
42. S. E. Harris, Electromagnetically induced transparency. *Phys. Today* **50**, 36 (1997).
43. S. Zhang, D. A. Genov, Y. Wang, M. Liu, X. Zhang, Plasmon-induced transparency in metamaterials. *Phys. Rev. Lett.* **101**, 047401 (2008).
44. Y. Yang, I. I. Kravchenko, D. P. Briggs, J. Valentine, All-dielectric metasurface analogue of electromagnetically induced transparency. *Nat. Commun.* **5**, 5753 (2014).
45. M. F. Limonov, M. V. Rybin, A. N. Poddubny, Y. S. Kivshar, Fano resonances in photonics. *Nat. Photonics* **11**, 543 (2017).
46. L. Cong *et al.*, All-optical active THz metasurfaces for ultrafast polarization switching and dynamic beam splitting. *Light Sci. Appl.* **7**, 28 (2018).
47. J. Lou *et al.*, Optically controlled ultrafast terahertz metadevices with ultralow pump threshold. *Small* **17**, e2104275 (2021).
48. L. Cong, J. Han, W. Zhang, R. Singh, Temporal loss boundary engineered photonic cavity. *Nat. Commun.* **12**, 6940 (2021).
49. J. Yu *et al.*, Electrically tunable nonlinear polaritonic metasurface. *Nat. Photonics* **16**, 72 (2022).
50. M. Wuttig, H. Bhaskaran, T. Taubner, Phase-change materials for non-volatile photonic applications. *Nat. Photonics* **11**, 465 (2017).
51. Y. Wang *et al.*, Electrical tuning of phase-change antennas and metasurfaces. *Nat. Nanotechnol.* **16**, 667–672 (2021).
52. Y.-Y. Xie *et al.*, Metasurface-integrated vertical cavity surface-emitting lasers for programmable directional lasing emissions. *Nat. Nanotechnol.* **15**, 125–130 (2020).
53. Y. Huang, P. Sun, Z. Zhang, C. Jin, Numerical method based on transfer function for eliminating water vapor noise from terahertz spectra. *Appl. Opt.* **56**, 5698–5704 (2017).